Computers and Geotechnics 134 (2021) 104052

Contents lists available at ScienceDirect

Computers and Geotechnics

journal homepage: www.elsevier.com/locate/compgeo

Research Paper

A polybézier-based particle model for the DEM modeling of granular media

Zhengshou Lai [a], Linchong Huang [b,*]

[a] School of Intelligent Systems Engineering, Sun Yat-sen University, Shenzhen 518107, China
[b] School of Aeronautics and Astronautics Engineering, Sun Yat-sen University, Shenzhen 518107, China

ARTICLE INFO

Keywords:
Discrete element method
Particle model
Polybézier curve
GJK and EPA algorithms
Geometric fitting

ABSTRACT

The discrete element method (DEM) has become a prominent tool for modeling granular media, whereas the development of versatile and efficient particle models for the modeling of irregular-shaped particles remains a heated topic and challenge. In this work, a new particle model based on polybézier curves to describe particle shapes is proposed for the modeling of smooth and irregular-shaped particles. In particular, cubic bézier curves are adopted because they have a fairly high degree of freedom in modeling curved geometries as well as a closed-form support function. With the particle geometry and support function derived from cubic polybézier curves, the Gilbert-Johnson-Keerthi algorithm is adopted to detect contacts, and the expanding polytope algorithm is adopted to resolve contact geometric features. To generate polybézier-based particle templates from images of particle shapes, a particle swarm optimization-based geometric fitting procedure is also developed. The effectiveness of the proposed particle model for shape representation is validated using a chart of particle shapes with various roundness and sphericity characteristics. DEM simulations of random packing and biaxial compression tests on polydispersed irregular-shaped particles are also presented, and the results show that the proposed model has fairly good computational efficiency and numerical stability.

1. Introduction

Granular materials, such as ore, sand and grain, are generally nonspherical in nature. Particle irregularity has been well recognized to have substantial effects on the macroscopic properties, such as the packing density, stiffness and strength, of a granular medium. For example, laboratory experiments have shown that the increase in the particle irregularity (e.g., decrease in the sphericity and/or roundness) would lead to an increase in the extreme void ratios, decrease in the small-strain stiffness, increase in the compressibility, increase in the critical state line intercept, etc. (Cho et al., 2006) A prominent numerical tool for modeling granular media is the discrete element method (DEM) (Cundall and Strack, 1979), which has been used for many applications in a wide range of engineering disciplines (e.g., (Cleary and Sawley, 2002; Zhu et al., 2008; Lisjak and Grasselli, 2014; Xia et al., 2020)). To create an accurate and predictive DEM model for a granular medium, a critical step is to incorporate the shape irregularity of the constituent particles.

Over the years, many particle models have been developed to account for different types of particle shapes. For example, particle models have been developed based on ellipsoids (Lin and Ng, 1997), polyellipsoids (Munjiza et al., 2009), superquadrics (Cleary and Sawley, 2002; Podlozhnyuk et al., 2017), cylinders (Feng et al., 2017), polyhedrons (Zhao et al., 2015), nonuniform rational basis splines (NURBS) (Andrade et al., 2012; Lim and Andrade, 2014), and Fourier series (Lai et al., 2020). In any of these models, the particle shape is represented by a continuous function or a series of discrete functions, and the contact detection and resolution problem is solved using numerical optimization methods such as Newton's method (Andrade et al., 2012; Lai et al., 2020), the Levenberg–Marquardt method (Zhao and Zhao, 2019), the Nelder-Mead simplex algorithm (Zhao and Zhou, 2017), and the Gilbert-Johnson-Keerthi (GJK) algorithm (Wachs et al., 2012; Rakotonirina et al., 2019). Generally, the aforementioned particle models are categorized as the single-particle approach (Zhong et al., 2016). Another option to model irregular-shaped particles is the composite-particle approach, in which an irregular-shaped particle is represented by a clump of simple geometries, such as spheres or circles (Lai and Chen, 2017; Zheng and Hryciw, 2017; Nie et al., 2020). Compared with the single-particle approach, the composite-particle approach has the disadvantage of low computational efficiency and unrealistic contact parameters (Pereira et al., 2011; Navarro and de Souza Braun, 2013; Zheng and Hryciw, 2017). Thus, the single-particle approach has

* Corresponding author
E-mail address: hlinch@mail.sysu.edu.cn (L. Huang).

https://doi.org/10.1016/j.compgeo.2021.104052
Received 2 September 2020; Received in revised form 17 January 2021; Accepted 31 January 2021
Available online 10 March 2021

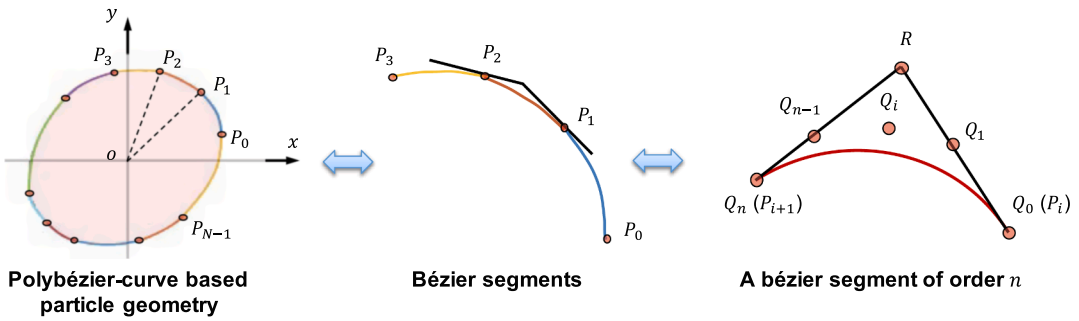

Fig. 1. Illustrative diagram of the polybézier-curve-based particle model.

recently received more interest and preference than the composite-particle approach for more accurate and predictive DEM models.

Despite the considerable number of well-developed particle models, interest in the development of irregular-shaped particle models is still growing for two reasons. First, the current particle models only cover a small portion of the various particle shapes that can be encountered in nature. Second, the corresponding contact detection and resolution algorithms generally require considerable implementation efforts. As a certain particle model would often require a certain contact detection and resolution algorithm, the implementation efforts are substantially increased if one would like to combine multiple particle models in one DEM simulation. Basically, when developing a particle model, three different factors need to be considered, namely, the accuracy, computational efficiency, and compatibility, whose relative importance depends on the aims of the users. The accuracy and computational efficiency are two factors that have an inverse relationship, and thus, as noted in Zhao and Zhao (2019), there is always a need to weigh a balance between the realistic approximation of particle shapes and the affordable computational efficiency for practical DEM modeling. The compatibility refers to the potential or capability of a new particle model to be integrated with the existing particle models. A particle model of high compatibility indicates that it is palatable to existing DEM code (particularly the contact detection and resolution algorithms) with no need to tangle with revising the DEM computational workflow or developing new contact algorithms. This aspect has been less considered in most previous studies.

In this work, a new particle model based on polybézier curves is proposed for the modeling of smooth and irregular-shaped particles. This new particle model can be regarded as an extension of the previously well-established polygon-based particle model (Mirghasemi et al., 2002) and NURBS-based particle model (Andrade et al., 2012), while it possesses two advantages with the use of polybézier curves to describe particle shapes. First, as bézier curves can describe curved geometries, the proposed polybézier-based particle model requires fewer segments than the polygon-based particle model to achieve the same shape representation accuracy. Second, as each bézier curve has its own control points, the polybézier-based particle model has greater flexibility for controlling the local curvatures of a particle shape compared with the NURBS-based particle model. In addition, the polybézier–based particle model has a closed-form expression of the support points. With the adoption of the classical GJK and Expanding Polytope Algorithm (EPA) to solve the contact detection and resolution problem, the polybézier-based particle model can be readily integrated with other existing particle models, such as the polygon-based particle model and ellipse-based particle model. This feature greatly increases the compatibility of the proposed polybézier-based particle model. It should be highlighted, however, that the proposed model is limited to convex shapes only and thus the discussion of this paper is also limited to convex irregular-shaped particles. In addition, this work has focused its discussion on two dimensions (2D) and the extension to three dimensions (3D) will be explored in future work.

The remainder of this paper is structured as follows. Section 2 presents the formulations of the polybézier-based particle model, including the particle geometry, support function, mass and moment of inertia. Section 3 describes the GJK and EPA algorithms employed to detect contacts and resolve contact geometric features. Section 4 introduces a particle swarm optimization (PSO)-based geometric fitting method for the generation of polybézier-based particle templates. Section 5 reports the results of numerical examples to demonstrate the performance of the polybézier-based particle model for shape representation and DEM simulation. Section 6 summarizes the concluding remarks of this work.

2. Polybézier-based particle model

2.1. Particle geometry

The polybézier-based particle model is composed of a set of bézier curves. Each bézier curve is a parametric curve with its own control points. Fig. 1 shows an illustrative diagram of the polybézier-based particle model. The particle geometry is described by N bézier segments, which are connected to each other at points $\boldsymbol{P_0}$,$\boldsymbol{P_1}$, …, $\boldsymbol{P_{N-1}}$. Particularly, to enhance the geometric continuity of the particle geometry, it is assumed that two neighboring bézier segments have the same tangent direction at the connecting point. In addition, the second and second to last control points of a bézier curve are imposed on the tangent lines at the end points. For example, segments $\boldsymbol{P_0P_1}$ and $\boldsymbol{P_1P_2}$ have the same tangent line at point $\boldsymbol{P_1}$, whereas segments $\boldsymbol{P_1P_2}$ and $\boldsymbol{P_2P_3}$ have the same tangent line at point $\boldsymbol{P_2}$. For each bézier segment (e.g., segment $\boldsymbol{P_iP_{i+1}}$), the second control point $\boldsymbol{Q_1}$ falls on line $\boldsymbol{RQ_0}$, which is the tangent line at point $\boldsymbol{Q_0}$; the second to last control point $\boldsymbol{Q_{n-1}}$ falls on line $\boldsymbol{RQ_n}$, which is the tangent line at point $\boldsymbol{Q_n}$; point $\boldsymbol{R}$ is the intersection of tangent lines $\boldsymbol{RQ_0}$ and $\boldsymbol{RQ_n}$ and n is the number of control points in each bézier curve. With these two constraints and by virtue of the nature of bézier curves, the G^1 continuity (i.e., surface and tangent continuity) of the whole particle geometry is achieved (Du and Schmitt, 1990). It is worth noting that, by a similar fashion, Wang et al. (2019) recently proposed a cubic-polynomial-curve-based approach to represent and generate convex particles, whereas the DEM implementation is not developed. The cubic-polynomial-curve-based particles were converted into circle-based composite particles for DEM simulation.

Technically, with sufficient segments and control points, the polybézier-based particle model is able to represent particles of arbitrary shapes. A typical case of the polybézier-based particle model is the polygon-based particle model, in which the order of the bézier segments is 1. However, the polygon-based particle model often requires a large number of segments to describe a particle with a curved and smooth geometry, and thus, it could be computationally expensive in DEM modeling. In the polybézier-based particle model, higher orders of bézier curves could be employed, which improves its flexibility to model curved geometries. A negative effect of higher orders of bézier curves is that they increase the difficulties in detecting contacts and resolving contact geometric features. In view of this issue, cubic bézier curves are

adopted in this work because they have analytic and closed-form expressions of the support points, which are important components of the GJK- and EPA-based contact algorithms. The formulation of the cubic bézier curves can be explicitly expressed as follows:

$$\boldsymbol{B}(t) = (1-t)^3\boldsymbol{Q_0} + 3(1-t)^2 t\boldsymbol{Q_1} + 3(1-t)t^2\boldsymbol{Q_2} + t^3\boldsymbol{Q_3}, \quad 0 \leqslant t \leqslant 1 \tag{1}$$

where $\boldsymbol{B}(t)$ represents the points on the bézier curve, t is a parametric parameter, and $\boldsymbol{Q_0}, \boldsymbol{Q_1}, \boldsymbol{Q_2}$ and $\boldsymbol{Q_3}$ are the control points. To facilitate the implementation of the polybézier-based particle model, cubic bézier curves can also be formulated in matrix form as

$$\boldsymbol{B}(t) = [\boldsymbol{Q_0} \quad \boldsymbol{Q_1} \quad \boldsymbol{Q_2} \quad \boldsymbol{Q_3}] \begin{bmatrix} 1 & -3 & 3 & -1 \\ 0 & 3 & -6 & 3 \\ 0 & 0 & 3 & -3 \\ 0 & 0 & 0 & 1 \end{bmatrix} \begin{bmatrix} 1 \\ t \\ t^2 \\ t^3 \end{bmatrix} \tag{2}$$

where the control points $\boldsymbol{Q_0}, \boldsymbol{Q_1}, \boldsymbol{Q_2}$ and $\boldsymbol{Q_3}$ are expressed as column vectors.

2.2. Support lines and support points

Support lines and support points of a particle geometry are important components in many contact detection and resolution algorithms (Ghosh and Kumar, 1998; Kenwright, 2015). In computational geometry, a supporting line (or supporting hyperplane in higher-dimensional space) of convex geometry A is a line that has both of the following properties: A is entirely contained in one of the two closed half-spaces bounded by the line, and A has at least one boundary-point on the line. A support point is the point that lies on geometry A as well as on the support line. It has the highest dot production with the given support direction. Mathematically, a support point can be expressed as a function of the support direction, such that

$$s_A(\boldsymbol{v}) = \text{argmax}_{\boldsymbol{P_A}} \boldsymbol{P_A} \cdot \boldsymbol{v}, \boldsymbol{P_A} \in \boldsymbol{A} \tag{3}$$

where $s_A(\boldsymbol{v})$ represents the support point in support direction $\boldsymbol{v}$, and $\boldsymbol{P_A}$ represents a point on geometry A.

In the polybézier-based particle model, support points can be given by

$$s_A(\boldsymbol{v}) = \boldsymbol{B}(t_v) \tag{4}$$

where t_v is the parametric parameter that corresponds to support direction $\boldsymbol{v}$. By definition, the support lines are perpendicular to the support directions, such as

$$\boldsymbol{v} \cdot \boldsymbol{B}'(t_v) = \boldsymbol{0} \tag{5}$$

where $\boldsymbol{B}'(t_v)$ is the derivative of $\boldsymbol{B}(t)$ at t_v and represents the direction of the support lines. Recalling Eq. (2), the derivative $\boldsymbol{B}'(t)$ is given as

$$\boldsymbol{B}'(t) = [\boldsymbol{Q_0} \quad \boldsymbol{Q_1} \quad \boldsymbol{Q_2} \quad \boldsymbol{Q_3}] \begin{bmatrix} 1 & -3 & 3 & -1 \\ 0 & 3 & -6 & 3 \\ 0 & 0 & 3 & -3 \\ 0 & 0 & 0 & 1 \end{bmatrix} \begin{bmatrix} 0 \\ 1 \\ 2t \\ 3t^2 \end{bmatrix} \tag{6}$$

Substituting Eq. (6) into Eq. (5) and rearranging the terms gives

$$3M_4 t_v^2 + 2M_3 t_v + M_2 = 0 \tag{7}$$

where

$$\boldsymbol{M} = [M_1 \quad M_2 \quad M_3 \quad M_4] = \boldsymbol{v} \cdot [\boldsymbol{Q_0} \quad \boldsymbol{Q_1} \quad \boldsymbol{Q_2} \quad \boldsymbol{Q_3}] \begin{bmatrix} 1 & -3 & 3 & -1 \\ 0 & 3 & -6 & 3 \\ 0 & 0 & 3 & -3 \\ 0 & 0 & 0 & 1 \end{bmatrix} \tag{8}$$

where M_1, M_2, M_3 and M_4 represent the components of vector $\boldsymbol{M}$. Eq. (7) is a quadratic function, which has a closed-form solution given as

$$t_v = \frac{-2M_3 \pm \sqrt{4M_2^2 - 12M_4M_2}}{6M_4} \tag{9}$$

where the solution that falls in the range of [0, 1] will be adopted. With the solution t_v, the support point corresponding to support direction $\boldsymbol{v}$ can be calculated from Eq. (4).

2.3. Mass and moment of inertia

The mass and moment of inertia are estimated from a polygon that is interpolated from the polybézier curves. For each bézier curve, a series of boundary points can be obtained with a parametric sweep of parameter t. Assuming that the interpolated points are (x_0, y_0), (x_1, y_1), …, (x_{n-1}, y_{n-1}), which form a polygon without self-intersection, the mass and moment of inertia can be calculated as

$$m = \frac{\rho}{2} \sum_{i=0}^{n-1} (x_i y_{i+1} - x_{i+1} y_i) \tag{10}$$

$$I = \frac{\rho}{12} \sum_{i=0}^{n-1} (x_i y_{i+1} - x_{i+1} y_i)(x_i^2 + x_i x_{i+1} + x_{i+1}^2 + y_i^2 + y_i y_{i+1} + y_{i+1}^2) \tag{11}$$

where m and I represent the mass and moment of inertia, respectively, ρ is the particle density, $x_n = x_0$ and $y_n = y_0$. By a slight abuse of notation, parameter n herein represents the number of interpolated boundary points. It should be noted that although an interpolated polygon is used to estimate the mass and moment of inertia, the estimates of the mass and moment of inertia would approach the exact values if the interpolation is dense. In addition, the computational efficiency of a DEM simulation would not be impacted as the mass and moment of inertia only need to be calculated once.

3. Contact detection and resolution algorithms

The detection and resolution of particle contacts are the most time-consuming steps of a DEM cycle. Usually, contact detection is implemented with two phases, i.e., the broad phase and the narrow phase (Hubbard, 1995; Mirtich, 1997). In the broad phase, contact tests are performed on the bounding volumes (e.g., bounding spheres or bounding boxes) of particles to quickly prune away the pairs of particles that are not in contact with each other (Luque et al., 2005; Pouchol et al., 2009). In the narrow phase, contact tests are performed on the exact geometries of the particles. In this work, the classical GJK and EPA algorithms are adopted to detect contacts and resolve contact geometric features for the proposed polybézier-based particle model. For the sake of completeness, the GJK and EPA algorithms are briefly described in this section. It is worth noting that there are other contact detection and resolution algorithms with higher performance than the adopted GJK and EPA algorithms. One good candidate for contact detection is the hybrid Levenberg–Marquardt and GJK approach (Zhao and Zhao, 2019). It can as well be adopted to solve the contact resolution problem with the aid of a shape erosion strategy. In this work, the classical GJK and EPA algorithms are adopted for simplicity and it is noted that the proposed polybézier-based particle model is also applicable to those improved GJK-based algorithms.

3.1. Contact detection: GJK algorithm

The GJK algorithm is a fast procedure for computing the distance between convex objects in 2D or 3D space. It was first introduced by Gilbert et al. (1988) and has since been popularly applied in fields such as robotics, computer-aided design and computer graphics. The employment of the GJK algorithm to address the contact detection problem in DEM has recently emerged, and Wachs et al. (2012), Zhao

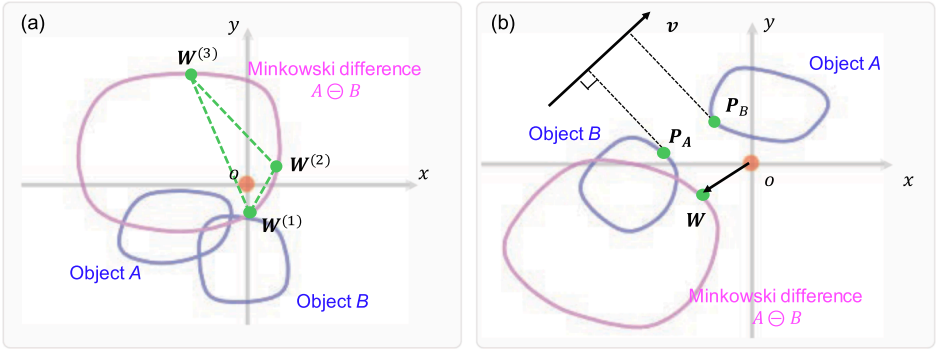

Fig. 2. The contact detection and convergence criteria of the GJK algorithm. In scenario (a), two objects are in contact as the Minkowski difference contains the origin. The GJK algorithm converges with a contact flag if the built simplex contains the origin. In scenario (b), two objects are not in contact, as the Minkowski difference does not contain the origin. The GJK algorithm converges with a noncontact flag if a support point is in opposite to the searching direction.

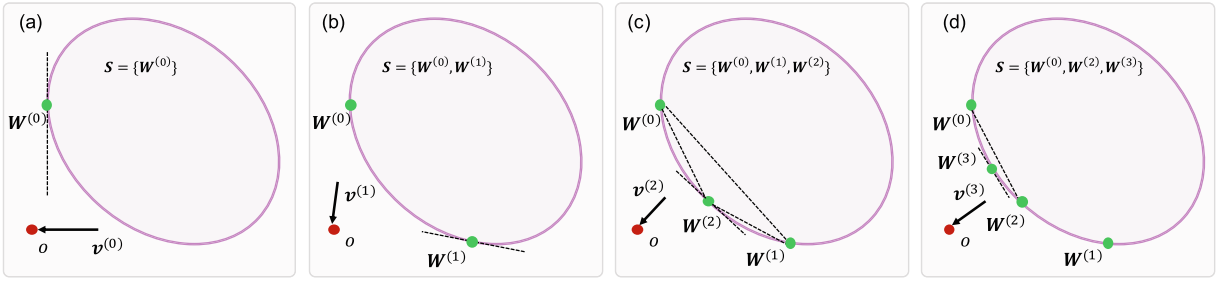

Fig. 3. Illustrative diagram of the procedures of the GJK algorithm.

and Zhao (2019) are among the first efforts.

The GJK algorithm relies heavily on the Minkowski difference. Given two objects A and B, the Minkowski difference is defined as a set of pairwise differences of all points from A and B (Hadwiger, 1950):

$$A\Theta B = \{\boldsymbol{P_A} - \boldsymbol{P_B} | \boldsymbol{P_A} \in \boldsymbol{A}, \boldsymbol{P_B} \in \boldsymbol{B}\} \tag{12}$$

where $A\Theta B$ denotes the Minkowski difference of A and B; $\boldsymbol{P_A}$ and $\boldsymbol{P_B}$ denote the points in A and B, respectively. If both objects are convex, the corresponding Minkowski difference is also convex. With the use of the Minkowski difference, the contact detection problem becomes equivalent to determining whether the Minkowski difference contains the origin. As illustrated in Fig. 2, if the Minkowski difference contains the origin, the two objects are in contact; and if the Minkowski difference does not contain the origin, the two objects are not in contact.

In the GJK algorithm, the exact Minkowski difference is not computed. Instead, the simplex inside the Minkowski difference is iteratively built to attempt to enclose the origin. There are two convergence criteria in the GJK algorithm: if the built simplex contains the origin (as shown in Fig. 2(a)), the GJK algorithm converges with a contact flag; and if a support point in the Minkowski difference is in the opposite direction of the support direction (i.e., $\boldsymbol{v} \cdot \boldsymbol{W} < \boldsymbol{0}$ as shown in Fig. 2(b)), the GJK algorithm converges with a noncontact flag. The procedure of the GJK algorithm, as illustrated in Fig. 3, is described as follows (Gilbert et al., 1988; Ericson, 2004; Wachs et al., 2012).

1. Initialize an empty simplex S and randomly select an initial searching direction $\boldsymbol{v}$. A good practice for the initial searching direction could be the joint vector of the centroids of objects A and B.
2. Compute the support point $\boldsymbol{W}$ of the Minkowski difference in searching direction $\boldsymbol{v}$ and add it to the simplex S.
3. Check if this new support point $\boldsymbol{W}$ is in the opposite direction of the searching direction and return a noncontact flag if it is true.
4. Check if simplex S contains the origin and return a contact flag if it is true.
5. Compute the point $\boldsymbol{P}$ that is nearest to the origin in simplex S and reduce S to the smallest subset that contains $\boldsymbol{P}$. That is, remove any points in S not determining the subsimplex of S in which $\boldsymbol{P}$ lies.
6. Let vector $-\boldsymbol{P}$ be the new searching direction $\boldsymbol{v}$.
7. Repeat steps (2–6) until a convergence criterion or a maximum number of iterations is reached.

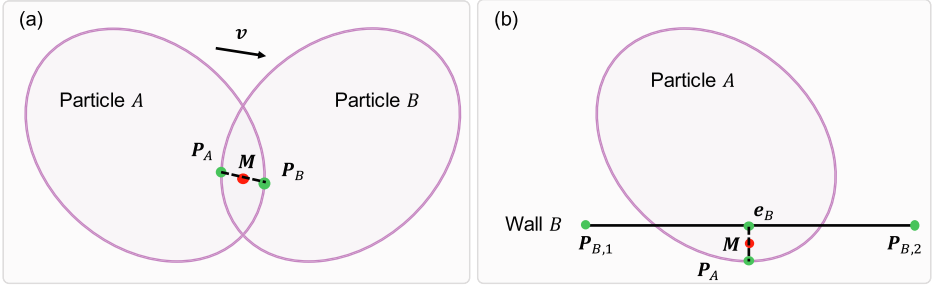

Fig. 4. Definition of the contact geometric features based on the EPA.

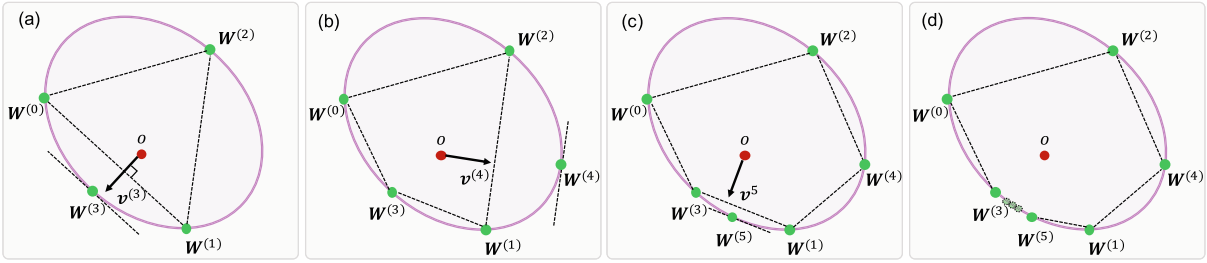

Fig. 5. Illustrative diagram of the procedures of the EPA.

3.2. Contact resolution: EPA

The GJK algorithm can only return the contact flag and the distance if two objects are not in contact. The EPA is further implemented to determine the contact geometric features such as the penetration depth and contact point. Fig. 4 illustrates the definition of the contact penetration depth and contact point. Using the Minkowski difference, the penetration depth can be given as

$$\delta_n = \min_{\boldsymbol{v}} \boldsymbol{v} \cdot [\boldsymbol{s}_A(\boldsymbol{v}) - \boldsymbol{s}_B(-\boldsymbol{v})] \tag{13}$$

where δ_n represents the penetration depth, and $\boldsymbol{s}_A(\boldsymbol{v}) - \boldsymbol{s}_B(-\boldsymbol{v})$ represents a support point on the Minkowski difference of objects A and B. With the direction that gives the smallest dot production, the corresponding support points on objects A and B can be calculated. The contact point is then defined and calculated as the middle point of these two support points, as shown in Fig. 4(a). For a particle–wall contact, the support point of the wall may be returned as the end points of the wall, which would lead to a spurious contact point. In this case, the foot point of the perpendicular line passing the support point of the particle is first determined. The contact point is then defined as the middle point of the foot point and the support point, as shown in Fig. 4(b).

In the EPA, a polytope is created inside of the Minkowski difference of two objects and iteratively expanded until it approaches the support point on the Minkowski difference that is closest to the origin. Fig. 5 illustrates the main procedures of the EPA. With a polytope (or simplex) that contains the origin, the polytope is gradually expanded by iteratively adding support points in the direction of the point nearest to the origin in the polytope. For example, in Fig. 5(a-c), the point nearest to the origin in the polytope lines in simplex $\boldsymbol{W}^{(0)}\boldsymbol{W}^{(1)}$, $\boldsymbol{W}^{(1)}\boldsymbol{W}^{(2)}$ and $\boldsymbol{W}^{(1)}\boldsymbol{W}^{(3)}$, respectively. The newly added points $\boldsymbol{W}^{(3)}$, $\boldsymbol{W}^{(4)}$ and $\boldsymbol{W}^{(5)}$ of the polytope are the support points in the directions perpendicular to these simplices. An initial polytope usually has three points, which can be obtained from the GJK algorithm during the contact detection process. The iteration is considered to converge if the difference between the norm of the newly added support point and the smallest distance from the origin to the edges of the polytope is within an acceptable tolerance, which is similar to the convergence criterion of the GJK for calculating the distance between two non-colliding objects (Bergen, 1999).

4. Generation of polybézier-based particle templates

With the developed polybézier-based particle model, the next step for practical DEM modeling is the generation of polybézier-based particles that conform to a realistic particle morphology. A general approach to obtain the realistic morphological features of a granular material is to use the imaging techniques, including photography (Zheng et al., 2017), scanning electron microscopy (Cox and Budhu, 2008), and X-ray computed tomography (CT) (Desrues et al., 2010; Thakur and Penumadu, 2020). The first two techniques only provide 2D morphological information (i.e., 2D images), which, however, can be used to approximate or infer 3D morphological features, e.g., through a virtual

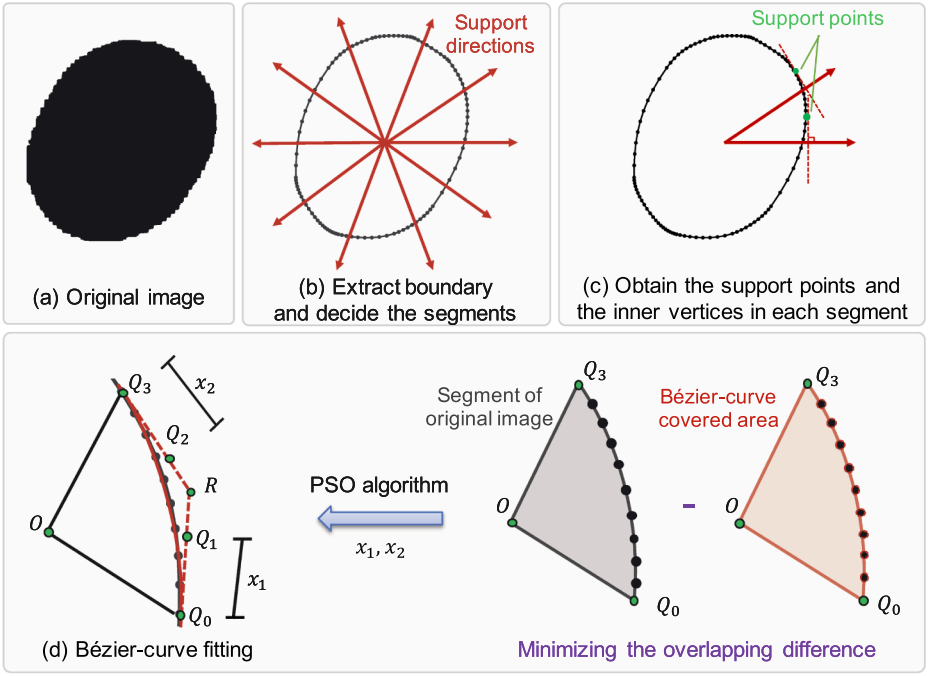

Fig. 6. Illustrative diagram of the PSO-based geometric fitting procedure for generating polybézier-based particles from images of particle shapes.

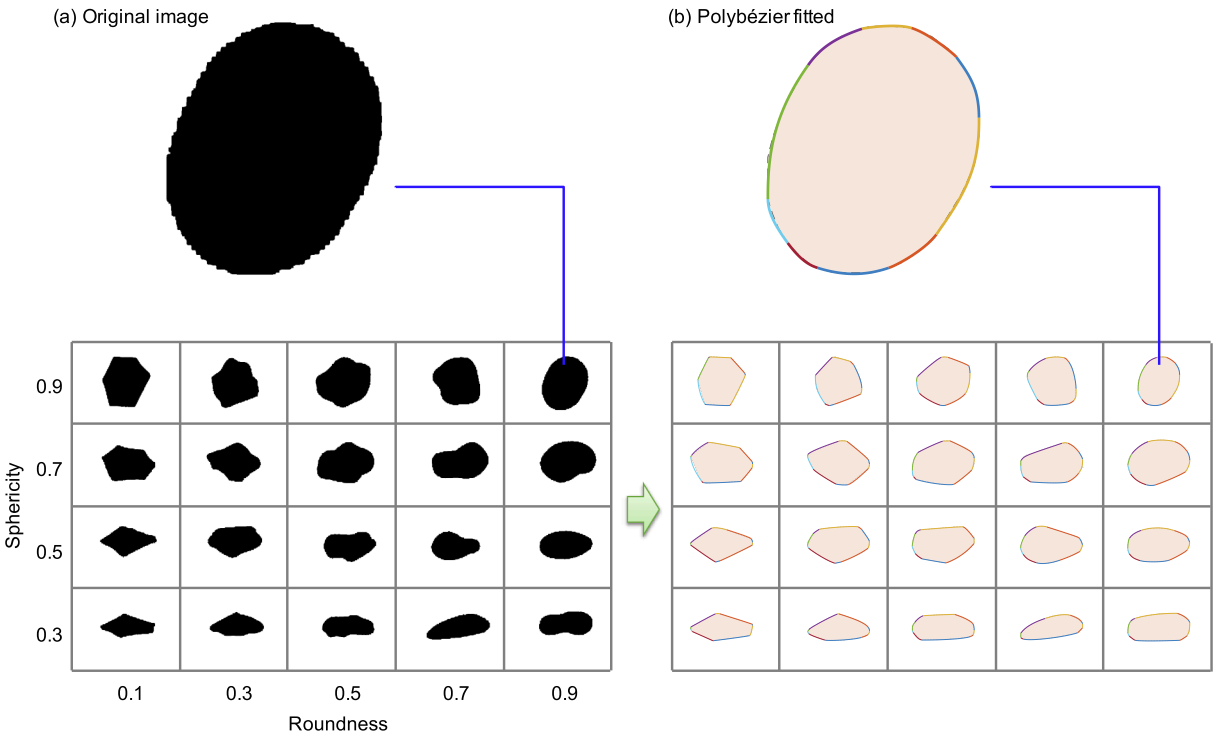

Fig. 7. Examples of particle shapes with different roundness and sphericity characteristics: (a) particle shapes represented by images (adapted from (Krumbein and Sloss, 1951)), and (b) particle shapes represented by polyb.ézier curves.

3D surface method (Mollon and Zhao, 2013) or through enhancing the illusion of the depth of 2D images (Zheng and Hryciw, 2017). X-ray CT, on the other hand, can be used to directly obtain 3D morphological information and therefore has been the most prevalent technique in recent years (Matsushima et al., 2009; Garboczi, 2011; Andò et al., 2013; Vlahinić et al., 2014; Zhou et al., 2018). The particle shapes represented by images cannot be directly used in DEM modeling. They need to be transformed into particle templates using particle models. This section introduces a PSO-based geometric fitting approach for generating polybézier-based particle templates from the images of the particle shapes.

In the case of the polybézier-based particle model, the particle shape is represented by a set of bézier curves. To generate a polybézier-based particle template, the most important step is to determine the coordinates of the control points of each bézier curve. With particle shapes captured in images, the problem becomes finding the optimal coordinates of the control points so that the particle shape represented by the bézier curves can cover the shape represented by the image with high accuracy. For such a purpose, a PSO-based geometric fitting procedure is developed in this section. PSO is an iterative stochastic algorithm that is based on social-psychological principles. It was originally proposed by Eberhart and Kennedy (1995) and Eberhart et al. (1996) and has been used across a wide range of applications, such as image and video analysis, control applications, and system identification Van den Bergh and Engelbrecht (2010), Poli et al. (2007). Its application in the geomechanics community is rare, and recent efforts along this line include the work by Feng et al. (2006) for identifying parameters in constitutive models and Lai and Chen (2017) for material bifurcation analysis. Fig. 6 shows an illustrative diagram of the PSO-based geometric fitting procedure for generating polybézier-based particle templates from images of particle shapes. The procedure is described as follows.

1. With the image of a single particle, extract the boundary points of the particle and find the convex hull of the boundary points.
2. Given the number of the bézier curve segments, determine the support directions at the ends of each bézier curve. In this work, uniformly spaced support directions are adopted, as shown in Fig. 6(b).
3. Find the support points of every support direction and use these support points as the segmentation locations to divide the boundary points into subsets (see Fig. 6(c)).
4. For each subset of boundary points, the PSO algorithm is used to find the optimal coordinates of the control points so that the bézier curve would fit the boundary points with high accuracy. A subroutine of the PSO fitting procedure is described as follows (see Fig. 6(d)).
   (a) For each segment, find the intersect $\boldsymbol{R}$ of lines $\boldsymbol{Q_0Q_1}$ and $\boldsymbol{Q_2Q_3}$, where lines $\boldsymbol{Q_0Q_1}$ and $\boldsymbol{Q_2Q_3}$, respectively, are the tangent lines at the ends (i.e., $\boldsymbol{Q_0}$ and $\boldsymbol{Q_3}$) of this segment. The tangent lines can be obtained by drawing lines that pass the ends and are perpendicular to the support directions at the ends.
   (b) Define the variables x_1 and x_2, which are the lengths of line segments $\boldsymbol{Q_0Q_1}$ and $\boldsymbol{Q_2Q_3}$, respectively, and define the cost, which is the overlapping difference between the area covered by the original image and the area covered by the fitted bézier curve. In this work, the area covered by the original image or the fitted bézier curves is obtained through an imaging process. The particle shape represented by the bézier curves is first plotted on an image and then scaled to the same size as the image of the original shape. In the image, pixels inside the particle are labeled as ones, and pixels outside the particle segment are labeled zeros. The percent difference is then calculated as the number of pixels with different labels divided by the number of pixels labeled as ones.
   (c) Perform the PSO and determine the location of points $\boldsymbol{Q_1}$ and $\boldsymbol{Q_2}$ (i.e., the lengths x_1 and x_2 of line segments $\boldsymbol{Q_0Q_1}$ and $\boldsymbol{Q_2Q_3}$) by minimizing the cost (i.e., the overlapping difference).
5. Repeat the previous step until all the segments are fitted. If the accuracy is not sufficient, increase the number of segments and repeat this procedure.

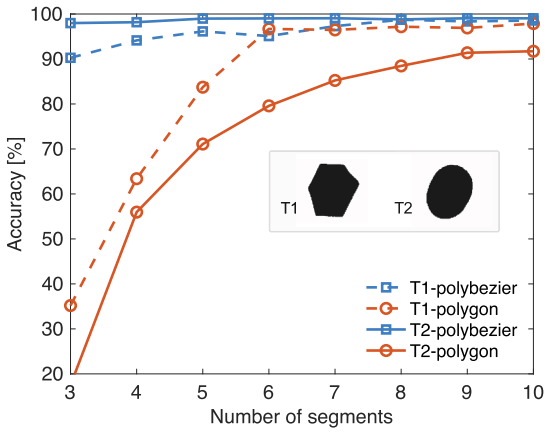

Fig. 8. The shape representation accuracy as a function of the number of segments.

5. Numerical examples

In this section, numerical examples are presented to demonstrate the performance of the proposed polybézier-based particle model. The accuracy of this particle model in representing various irregular-shaped particles is first investigated. Then, this particle model is implemented in an in-house DEM code, and DEM simulations of random packing and biaxial compression of polydispersed irregular-shaped particles are performed.

5.1. Model accuracy in shape representation

To investigate the accuracy of the proposed particle model in representing irregular-shaped particles, a chart of particle shapes with various roundness and sphericity characteristics, as shown in Fig. 7(a), is studied. This chart was originally developed by Krumbein and Sloss (1951) for characterizing particle roundness and sphericity. With the particle shapes represented by images, polybézier-based particle templates are generated following the PSO-geometric fitting procedure described in Section 4. In this example, 10 segments are adopted. Fig. 7 (b) shows the generated particle templates. Overall, the particle shapes represented by the polybézier curves match fairly well with those represented by the images.

To quantify the model accuracy of the proposed particle model in terms of shape representation, an accuracy score is defined as one minus the percent difference between the shape represented the particle model and the original image. The percent difference has been previously defined in Section 4 for the PSO-based geometric fitting procedure. Fig. 8 plots the model accuracy of the proposed particle model for two arbitrary particle shapes. As a comparison, the model accuracy of the polygon-based particle model is also presented. As the number of segments increases from 3 to 10, the accuracy of the polybézier-based particle model gradually increases and overall remains at 90% or higher. For the polygon-based particle model, generally more segments are required to achieve a compatible accuracy. Fig. 9 shows the evolution of the covered area using the polybézier-based particle model and polygon-based particle model. Compared with the polygon-based particle model, the effectiveness of the polybézier-based particle model in representing curved and smooth geometries can be effectively observed.

5.2. DEM simulation of random packing

The first example of DEM simulation considers the random packing of polydispersed irregular-shaped particles. In this example, a total of 500 noncircular particles are first randomly placed in a box of 1.0 m in width and 3.0 m in height and are then allowed to settle down under the influence of gravity. Specifically, these noncircular particles are represented by three different particle models, including the polybézier-based particle model, polygon-based particle model and ellipse-based particle model, to demonstrate the compatibility of the polybézier-based particle model with other conventional particle models. The polygon-based particles of 4∼ 7 line segments are used. The particles have an equivalent size that ranges from 40 mm to 60 mm. Herein, the equivalent size is defined as the diameter of the circle that has the same area as the

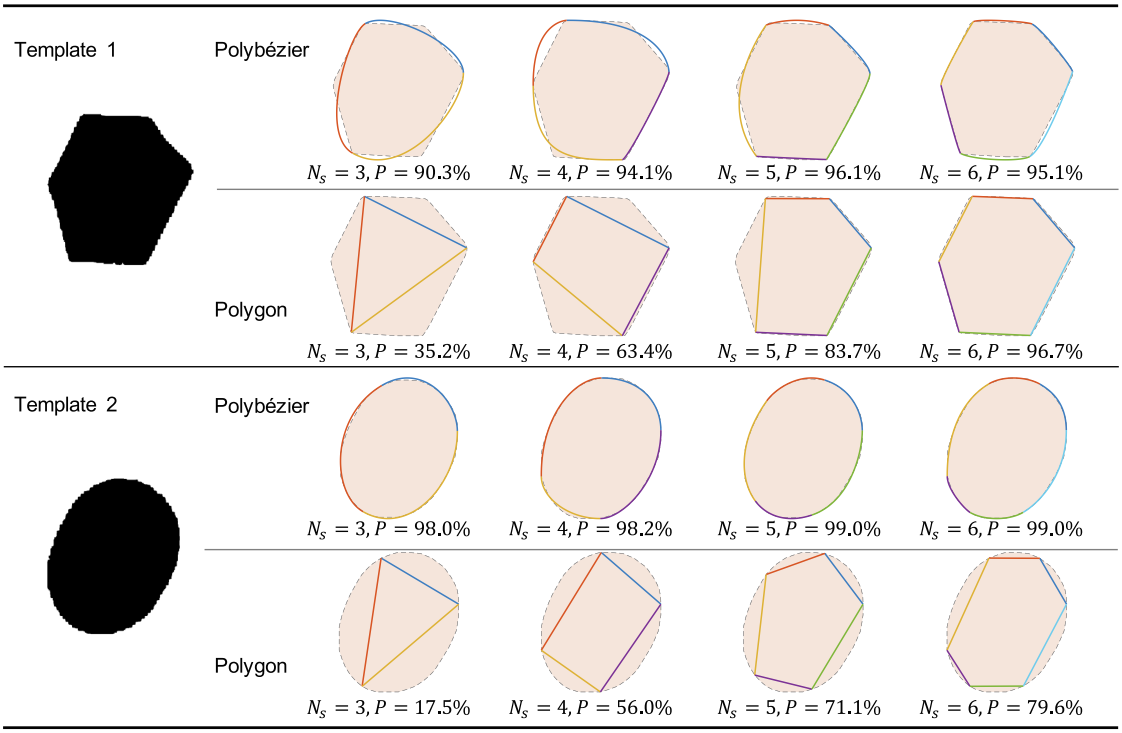

Fig. 9. Examples of particle shapes with different numbers of segments. N_s indicates the number of segments, and P indicates the shape representation accuracy.

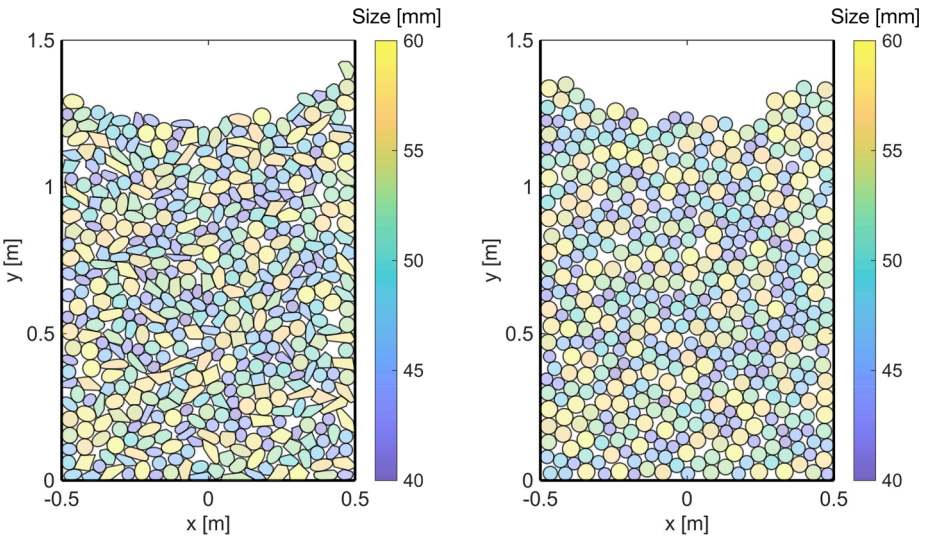

Fig. 10. Snapshots of the random packing simulation: (a) noncircular particles and (b) circular particles.

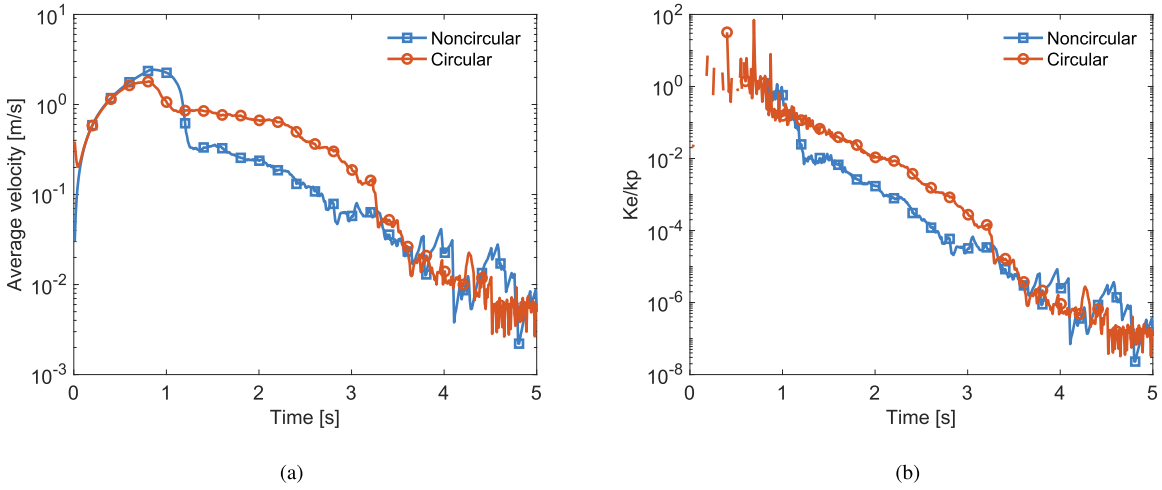

Fig. 11. Evolution of the (a) average velocity and (b) relative kinetic energy (i.e., the ratio of the kinetic energy to the contact potential energy).

particle. Throughout the packing process, the following parameters are used: the contact normal and tangential stiffness are 1×10^7 N/m, the contact friction is 0.2, and the damping is 0.7. A linear contact model is adopted. The contact friction is taken 0.2 according to the practical range found in the literature (Andrade et al., 2012; Senetakis et al., 2013; Nardelli et al., 2017; Zhao et al., 2018). For example, Senetakis et al. (2013) reported that the contact friction varies between 0.09 and 0.23 for quartz particles, while Nardelli et al. (2017) reported that it ranges between 0.25 and 0.37. The damping is introduced to facilitate the energy dissipation, and is taken the default value 0.7 suggested by the PFC (Itasca Consulting Group Inc, 2014). The simulation lasts for 5.0 s with a fixed time step of 1×10^{-4} s. As a comparison, the packing simulation with the same setup while using circular particles is also conducted.

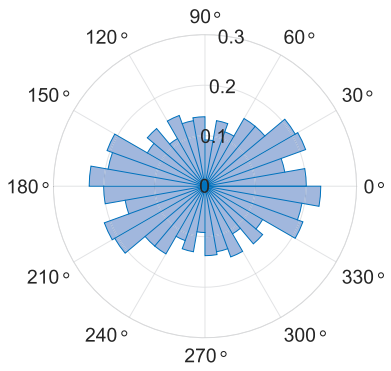

Fig. 12. Polar histogram of particle alignments for the noncircular particles case.

5.2.1. General packing characteristics

Fig. 10 compares the final particle assemblies for noncircular particles and circular particles, respectively. In both the noncircular and circular cases, the particles reside next to each other in the box without any visible spuriousness, such as unrealistic overlapping or floating particles. In the noncircular case, the contacts between the particles represented by different models (i.e., polybézier-based particle model, polygon-based particle model and ellipse-based particle) are all well detected by the GJK and EPA contact algorithms, indicating good

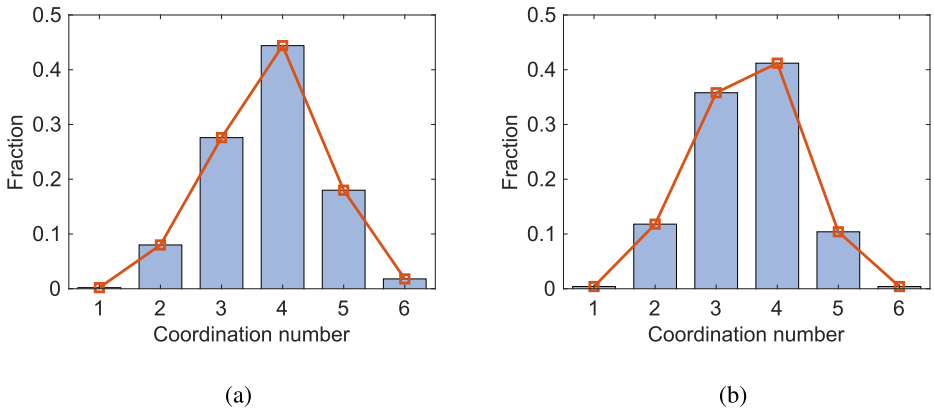

Fig. 13. Polar histogram of the coordination number: (a) noncircular particles and (b) circular particles.

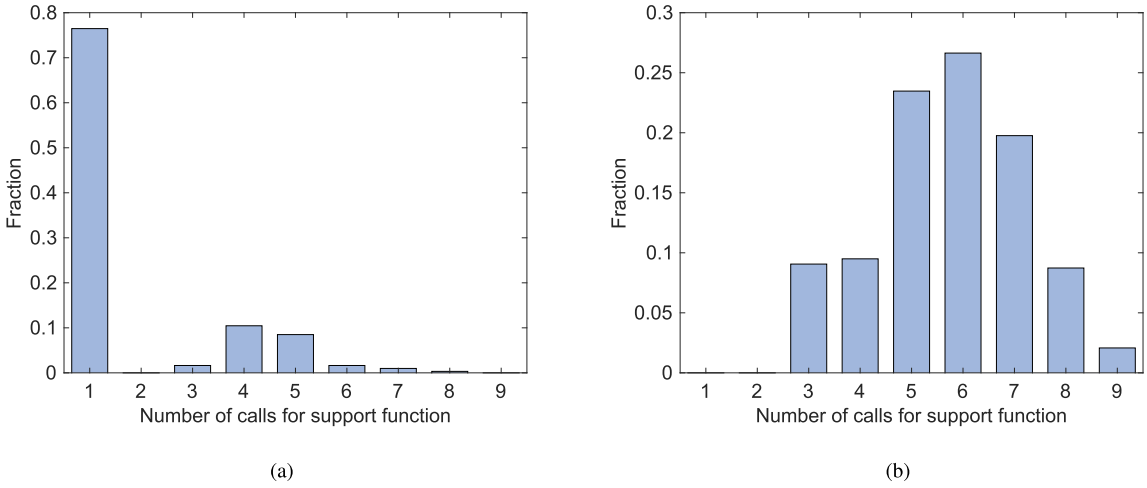

Fig. 14. Histogram of the number of calls for the support function in one computation cycle: (a) for pairs of particles that are not in contact and (b) for pairs of particles that are in contact.

compatibility of the polybézier-based particle model. Fig. 11 shows the evolution of the average particle translational velocity and the ratio of the kinetic energy to the contact potential energy (referred to as the relative kinetic energy hereafter) during the packing process. It can be observed that in both the noncircular and circular cases, the average velocity, as well as the relative kinetic energy, eventually decrease to small values, indicating a quasi-static equilibrium state. The evolution profiles of the particle velocity and kinetic energy indicate that the proposed polybézier-based particle model and the DEM implementation have good numerical stability.

As a quantitative analysis of the packing fabric, the alignments of the particles are calculated and plotted in Fig. 12. Herein, the alignment of a particle is defined as the angle from the x-axis to the particle major axis. For visualization purposes, the plot from 180° to 360° is also created by rotating the plot of particle alignment from 0° to 180° by 180°. With this treatment, a particle that aligns at θ is assumed to also align at θ+180°. The results in Fig. 12 indicate that the noncircular particles present a preference for horizontal alignment. This phenomenon is expected due to the shape irregularity effects.

In addition to the particle alignments, the coordination number of the particles is plotted and compared in Fig. 13. For noncircular particles, the coordination number ranges from 1 to 6 and is mostly 3, 4 or 5. For circular particles, the coordination number also ranges from 1 to 6 and is mostly 3 or 4. The results indicate that, at the end of random packing, the noncircular particles would have slightly more contacts than the circular particles.

5.2.2. *Computational performance*

The proposed polybézier-based particle model features two extras for computational efficiency. First, it is essentially developed to suit the fast GJK-based contact algorithms. Second, it is directly compatible with the conventional particle models, such as the circle-, ellipse-, or polygon-based ones, without the need to develop the particle model pair-wise contact algorithms. As different particle models have different performance, the computational efficiency can be improved by employing multiple particle models (e.g., simple circle-based particle model for those round-like particles and complex polybézier-based particle model for those irregular-shaped particles) in a DEM simulation. To investigate the computational performance of the proposed polybézier-based particle model, the convergence profiles of the GJK and EPA algorithms are analyzed. As described in Section 3.1, contact detection consists of a broad phase and a narrow phase. With the particle pairs that pass the broad-phase tests, the GJK algorithm is adopted to determine the exact contact flag. Fig. 14 plots the number of calls for the support function in the GJK algorithm in one computation cycle. It can be observed that the pairs of particles that are in contact overall require a larger number of calls for the support function than the particle pairs that are not in contact. Most of the noncontact pairs can be pruned away in one GJK iteration. The average number of calls for the support function is 1.85 for noncontact particle pairs and 5.77 for contact particle pairs.

To gain more insights into the computational performance of different particle models, the number of support function calls in the GJK algorithm for different types of particle pairs are listed in Table 1. In this table, the number of calls for noncontact pairs and contact pairs are

Table 1
Number of calls for the support function in the GJK algorithm for different types of particle model pairs.

Particle model	Ellipse	Polygon	Polybézier
Ellipse	5.33	4.48	5.72
Polygon	-	2.64	3.96
Polybézier	-	-	4.99

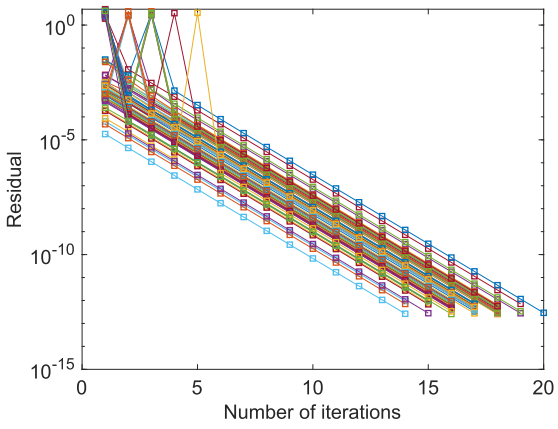

Fig. 15. The convergence profiles of the EPA for polybézier-based particles.

averaged altogether. The results indicate that for particles with continuous geometries (e.g., polybézier-based particles or ellipse-based particles), the number of support function calls is slightly larger than the polygon-based particles. However, it should be noted that the polygon-based particles in this example only have 4∼ 7 segments. The use of polybézier-based particles would not have a severe impact on the computational efficiency, while it could substantially improve the model accuracy for describing curved and smooth particle geometries.

Once a contact is detected by the GJK algorithm, the EPA is further invoked to find the penetration depth through an iteration process. Fig. 15 shows the convergence profile of the EPA for pairs of polybézier-based particles. Two primary observations can be made based on these results. First, the residual does not monotonically decrease with increasing number of iterations. The residual can exhibit a sudden increase. This phenomenon occurs in the scenario in which the polytope is expanded in a direction other than the direction of the minimal distance point. Second, the EPA with the polybézier-based particle model roughly follows a linear convergence trend. The slope of the convergence plot is approximately 6:10, which indicates that the residual will decrease by an order of 10^{-6} with 10 more iterations. In other words, the residual roughly decreases by one fourth in each iteration.

5.3. DEM simulation of biaxial compression

The second example of DEM simulation considers the biaxial compression test on polydispersed particles. Based on the random packing obtained in the previous section, the biaxial compression test proceeds with two stages: the consolidation stage and the compression stage. In the consolidation stage, the packing is consolidated with an isotropic pressure of 0.1 MPa. This is done by pushing the lateral walls and top wall inward until the target confining pressure is achieved. In the compression stage, the packing is compressed by moving the top wall downward at a velocity of 0.1 m/s while maintaining the lateral confining pressure at 0.1 MPa via a servo control mechanism. The consolidation stage lasts for 1.0 s, whereas the compression stage lasts for 2.0 s. The packing would finally have a compression strain of approximately 15%. The contact parameters and timestep are kept the same as those in the previous random packing example.

Fig. 16 shows snapshots of the particle assembly and contact force chain at the end of compression loading. In both the noncircular and circular cases, the particles exhibit a strong force chain in the vertical direction. Fig. 17 shows the evaluation of the deviatoric stress ratio and volumetric strain during the compression process. Herein, the following definition of stress invariants (i.e., p and q) and strains (i.e., ϵ_v and ϵ_a) in 2D are used Vardoulakis (1980), Chen et al. (2011), Zhao and Zhao (2019): $p = \sigma_a + \sigma_r, q = \sigma_a - \sigma_r, \epsilon_v = \log(H/H_0), \epsilon_v = \log(V/V_0)$, where H and V are the height and volume (i.e., area in the 2D case) of the specimen during shearing, respectively; H_0 and V_0 are their initial values before shear; and subscripts a and r indicate the axial and lateral directions, respectively. During the compression, the deviatoric stress ratio first increases rapidly and then gradually plateaus. The specimen of noncircular particles exhibits a larger shear strength than that of circular particles. As a more quantitative analysis, the fabric anisotropy of the particle packing after the end of the compression process is analyzed. The fabric anisotropy includes the anisotropies in the contact normal orientation, contact normal force, contact shear force, and contact branch orientation, which are closely related to the shear strength of a particle assembly (Voivret et al., 2009; Guo and Zhao, 2013; Li and Yu, 2014; Cheng et al., 2016; Gu et al., 2017; Sufian et al., 2017). The results of the contact normal orientation, contact normal force and contact shear force are shown in Fig. 18. For noncircular particles, the polar

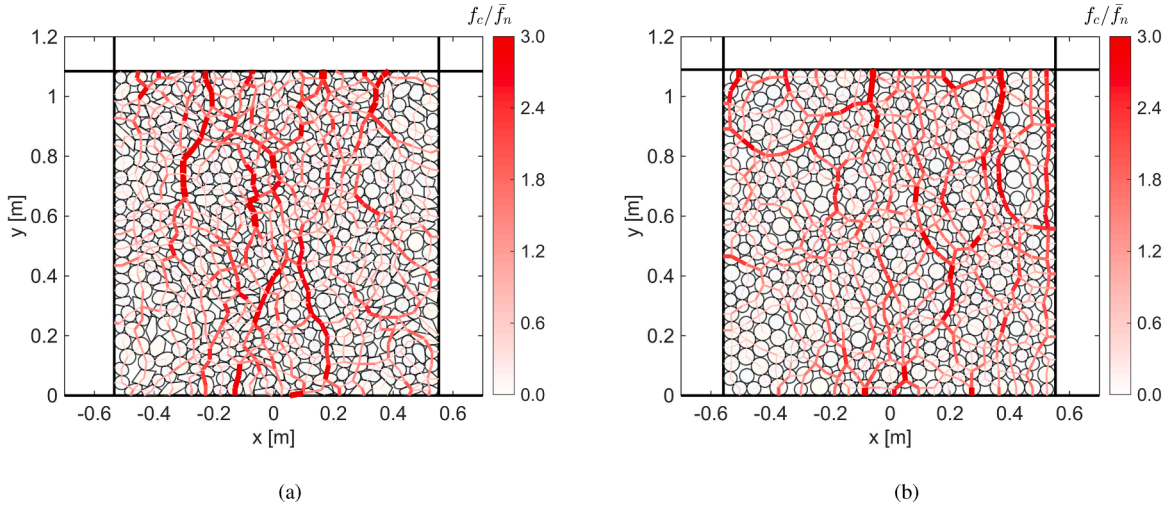

Fig. 16. Snapshots of the particle packing at the end of the compression process: (a) noncircular particles and (b) circular particles. The red solid lines represent the contact force chain. f_c and $\bar{f}_n$ indicate the magnitude of contact forces and the average magnitude of normal contact forces, respectively.

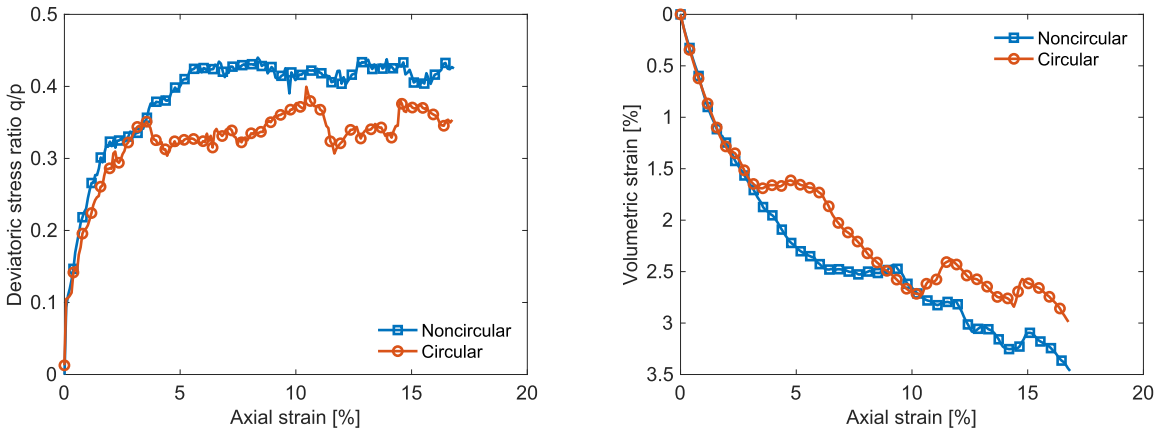

(a) (b)

Fig. 17. Evolution of the (a) deviatoric stress ratio and (b) volumetric strain during the biaxial compression process. The geomechanics sign convention of compression positive is adopted.

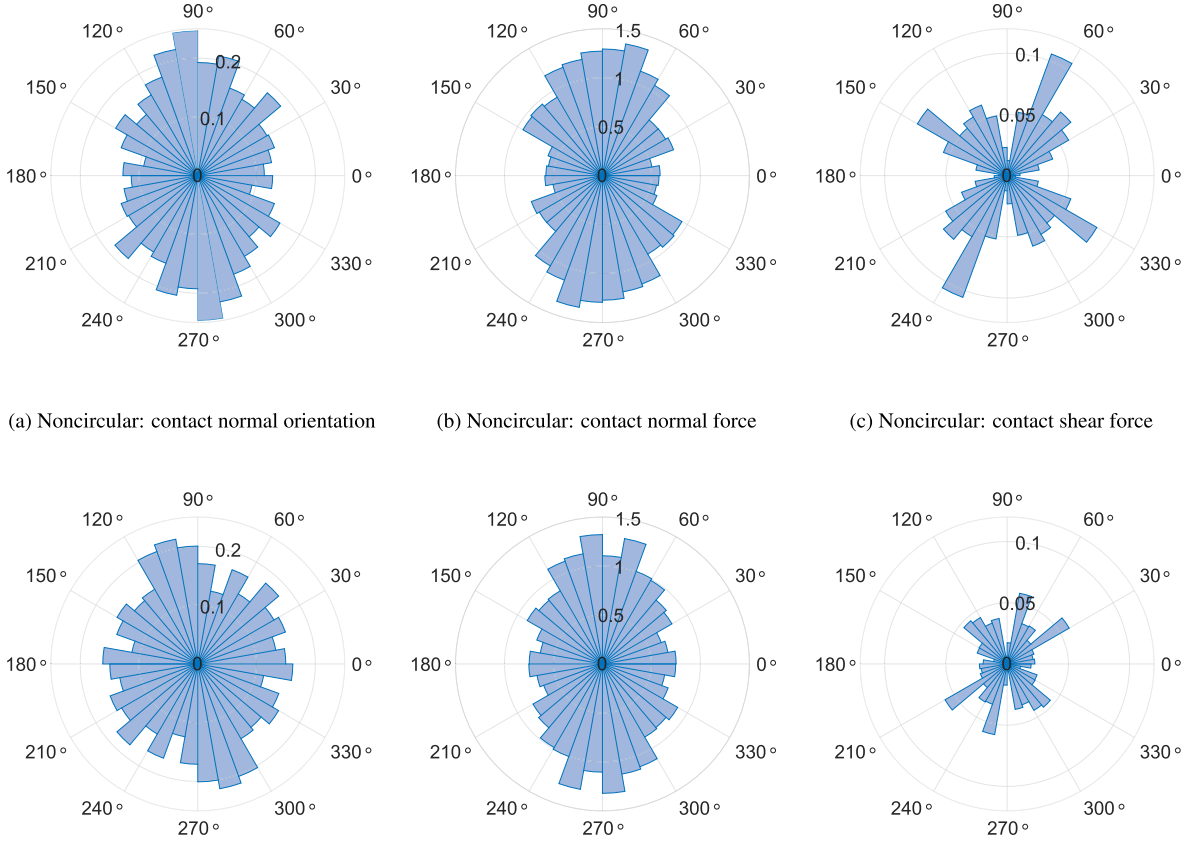

(a) Noncircular: contact normal orientation (b) Noncircular: contact normal force (c) Noncircular: contact shear force

(d) Circular: contact normal orientation (e) Circular: contact normal force (f) Circular: contact shear force

Fig. 18. Results of the packing anisotropies at the end of the biaxial compression process.

histograms of the contact normal orientation and contact normal force are more elongated in the vertical direction than circular particles. The noncircular particles also exhibit greater contact shear forces overall. As a result, the noncircular particles would finally exhibit a greater shear strength than the circular particles, which is consistent with the engineering experience that the particle shape irregularity has a substantial contribution to the shear strength of a particle assembly (Cho et al., 2006). Overall, the results demonstrate the good stability and effectiveness of the proposed particle model in a DEM simulation.

Lastly, it is noted that the polybézier-based particle model has the potential to be extended to 3D. Similar to the 2D case, the 3D polybézier-based particle model employs a set of joined bézier patches to describe particle geometry. Fig. 19 shows an example of the 3D polybézier-based particle template, which is composed of a number of 30 cubic bézier patches. With particle geometry represented by bézier patches, the support function, mass and moment of inertia could be derived, and the

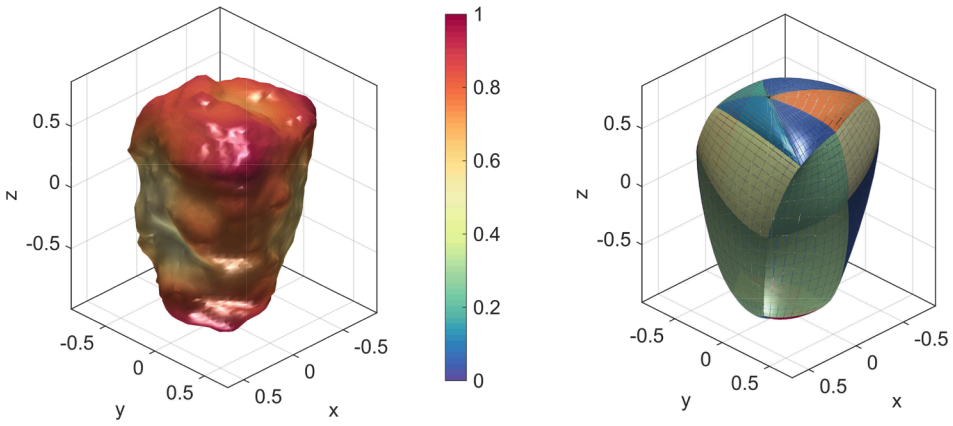

Fig. 19. An illustrative example of particle in 3D: (a) the original particle represented by a triangle mesh, where the color represents the distance for a surface point to the particle centroid, and (b) the generated particle template using the polybézier-based particle model, where the color is randomly selected for visualizing different bézier patches.

GJK and EPA algorithms could be adopted to solve the contact detection and resolution problem, following a framework similar to the 2D case. Nevertheless, there are several remaining challenges, including to develop a general scheme for the discretization of the surface patches, to come up with an efficient method for the parametrization of the support directions, to upgrade the PSO-based geometric fitting approach for generating 3D polybézier-based particle templates, and etc. In addition, the implementation of GJK and EPA in 3D is also fairly more complicated than the 2D case. These challenges will be explored in future work.

6. Summary

This paper presented a new polybézier-based particle model for the DEM modeling of smooth and irregular-shaped particles. In this particle model, the particle geometry is composed of a set of bézier curves. Each bézier curve has its own control points, whereas these bézier curves are connected at the ends, similar to polygons. Particularly, the bézier curves are assumed to share the same tangential directions at each connecting point so that the whole particle would have a geometric continuous support function. In addition, the cubic order of bézier curves is adopted in this work, as they have a fairly high degree of freedom in modeling curved geometries as well as have a closed-form support function. With the particle geometry and supporting function derived from cubic bézier curves, the GJK algorithm is adopted to detect contacts, and the EPA is adopted to resolve the contact geometric features. The adoption of the GJK and EPA enhances the compatibility of the proposed particle model with other existing particle models, such as the polygon-based particle model and ellipse-based particle model. With the proposed particle model, a PSO-based geometric fitting procedure for generating polybézier-based particle templates from images of particle shapes is also presented. The accuracy of the proposed particle model for shape representation is assessed using a chart of particle shapes with various roundness and sphericity characteristics. The results indicate that the proposed particle model is able to represent generally irregular-shaped particles with a fairly high accuracy. Finally, DEM simulations of random packing and biaxial compression tests of various irregular-shaped particles are also performed. The results of the DEM simulations have shown the good computational efficiency and numerical stability of the proposed particle model. The polybézier-based particle model has the potential to be extended to 3D, which will be explored in future work.

CRediT authorship contribution statement

Zhengshou Lai: Conceptualization, Methodology, Software, Investigation, Writing - original draft. **Linchong Huang:** Supervision, Writing - review & editing.

Declaration of Competing Interest

The authors declare that they have no known competing financial interests or personal relationships that could have appeared to influence the work reported in this paper.

Acknowledgment

The first author would like to acknowledge the support by the Hong Kong Scholars Program (2020). Both authors would like to acknowledge the support by the Fundamental Research Funds for the Central Universities (Grant No. 19lgpy289), the National Natural Science Foundation of China (51909289, 51978677), the China Postdoctoral Science Foundation (Grant No. 2019M663240, 2019M663239), and the Shenzhen Natural Science Foundation (Grant No. JCYJ20190807162401662).

References

Andò, E., Viggiani, G., Hall, S., Desrues, J., 2013. Experimental micro-mechanics of granular media studied by X-ray tomography: recent results and challenges. Géotech. Lett. 3 (3), 142–146.
Andrade, J.E., Lim, K.W., Avila, C.F., Vlahinić, I., 2012. Granular element method for computational particle mechanics. Comput. Methods Appl. Mech. Eng. 241, 262–274.
Bergen, G., 1999. A fast and robust GJK implementation for collision detection of convex objects. J. Graphics Tools 4 (2), 7–25.
Chen, Q., Andrade, J.E., Samaniego, E., 2011. AES for multiscale localization modeling in granular media. Comput. Methods Appl. Mech. Eng. 200 (33–36), 2473–2482.
Cheng, H., Yamamoto, H., Thoeni, K., 2016. Numerical study on stress states and fabric anisotropies in soilbags using the DEM. Comput. Geotech. 76, 170–183.
Cho, G.-C., Dodds, J., Santamarina, J.C., 2006. Particle shape effects on packing density, stiffness, and strength: natural and crushed sands. J. Geotech. Geoenviron. Eng. 132 (5), 591–602.
Cleary, P.W., Sawley, M.L., 2002. DEM modelling of industrial granular flows: 3D case studies and the effect of particle shape on hopper discharge. Appl. Math. Model. 26 (2), 89–111.
Cox, M., Budhu, M., 2008. A practical approach to grain shape quantification. Eng. Geol. 96 (1), 1–16.
Cundall, P.A., Strack, O.D.L., 1979. A discrete numerical model for granular assemblies. Géotechnique 29 (1), 47–65.
Desrues, J., Viggiani, G., Besuelle, P., 2010. Advances in X-ray Tomography for Geomaterials, vol. 118. John Wiley & Sons.
Du, W., Schmitt, F.J.M., 1990. On the G1 continuity of piecewise Bézier surfaces: a review with new results. Comput. Aided Des. 22 (9), 556–573.

Eberhart, R., Kennedy, J., 1995. A new optimizer using particle swarm theory. In: Proceedings of the Sixth International Symposium on Micro Machine and Human Science, vol. 1, New York, NY, pp. 39–43.
Eberhart, R., Simpson, P., Dobbins, R., 1996. Computational Intelligence PC Tools. Academic Press Professional, Inc.
Ericson, C., 2004. Real-time Collision Detection. CRC Press.
Feng, X., Chen, B., Yang, C., Zhou, H., Ding, X., 2006. Identification of visco-elastic models for rocks using genetic programming coupled with the modified particle swarm optimization algorithm. Int. J. Rock Mech. Min. Sci. 43 (5), 789–801.
Feng, Y.T., Han, K., Owen, D.R.J., 2017. A generic contact detection framework for cylindrical particles in discrete element modelling. Comput. Methods Appl. Mech. Eng. 315, 632–651.
Garboczi, E., 2011. Three dimensional shape analysis of JSC-1A simulated Lunar regolith particles. Powder Technol. 207 (1), 96–103.
Ghosh, P.K., Kumar, K.V., 1998. Support function representation of convex bodies, its application in geometric computing, and some related representations. Comput. Vis. Image Underst. 72 (3), 379–403.
Gilbert, E.G., Johnson, D.W., Keerthi, S.S., 1988. A fast procedure for computing the distance between complex objects in three-dimensional space. IEEE J. Robot. Automat. 4 (2), 193–203.
Gu, X., Hu, J., Huang, M., 2017. Anisotropy of elasticity and fabric of granular soils. Granular Matter 19 (2), 33.
Guo, N., Zhao, J., 2013. The signature of shear-induced anisotropy in granular media. Comput. Geotech. 47, 1–15.
Hadwiger, H., 1950. Minkowskische addition und subtraktion beliebiger punktmengen und die theoreme von Erhard Schmidt. Math. Z. 53 (3), 210–218.
Hubbard, P.M., 1995. Collision detection for interactive graphics applications. IEEE Trans. Visual Comput. Graphics 1 (3), 218–230.
Itasca Consulting Group Inc, 2014. PFC – Particle Flow Code, Ver. 5.0, Minneapolis: Itasca.
Kenwright, B., 2015. Generic Convex Collision Detection using Support Mapping, Tech. Rep.
Krumbein, W.C., Sloss, L.L., 1951. Stratigraphy and Sedimentation vol. 71, LWW.
Lai, Z., Chen, Q., 2017. Characterization and discrete element simulation of grading and shape-dependent behavior of JSC-1A Martian regolith simulant. Granular Matter 19 (4), 69.
Lai, Z., Chen, Q., 2017. Particle swarm optimization for numerical bifurcation analysis in computational inelasticity. Int. J. Numer. Anal. Meth. Geomech. 41 (3), 442–468.
Lai, Z., Chen, Q., Huang, L., 2020. Fourier series-based discrete element method for computational mechanics of irregular-shaped particles. Comput. Methods Appl. Mech. Eng. 362, 112873.
Li, X., Yu, H.-S., 2014. Fabric, force and strength anisotropies in granular materials: a micromechanical insight. Acta Mech. 225 (8), 2345–2362.
Lim, K.-W., Andrade, J.E., 2014. Granular element method for three-dimensional discrete element calculations. Int. J. Numer. Anal. Meth. Geomech. 38 (2), 167–188.
Lin, X., Ng, T.T., 1997. A three-dimensional discrete element model using arrays of ellipsoids. Géotechnique 47 (2), 319–329.
Lisjak, A., Grasselli, G., 2014. A review of discrete modeling techniques for fracturing processes in discontinuous rock masses. J. Rock Mech. Geotech. Eng. 6 (4), 301–314.
Luque, R.G., Comba, J.L.D., Freitas, C.M.D.S., 2005. Broad-phase collision detection using semi-adjusting BSP-trees, in. In: Proceedings of the 2005 Symposium on Interactive 3D Graphics and Games, pp. 179–186.
Matsushima, T., Katagiri, J., Uesugi, K., Tsuchiyama, A., Nakano, T., 2009. 3D shape characterization and image-based DEM simulation of the lunar soil simulant FJS-1. J. Aerospace Eng. 22 (1), 15–23.
Mirghasemi, A.A., Rothenburg, L., Matyas, E.L., 2002. Influence of particle shape on engineering properties of assemblies of two-dimensional polygon-shaped particles. Geotechnique 52 (3), 209–217.
Mirtich, B., 1997. Efficient algorithms for two-phase collision detection. Practical Motion Planning Robot.: Current Approaches Future Direct. 203–223.
Mollon, G., Zhao, J., 2013. Generating realistic 3D sand particles using Fourier descriptors. Granular Matter 15 (1), 95–108.
Munjiza, A., Peters, J.F., Hopkins, M.A., Kala, R., Wahl, R.E., 2009. A poly-ellipsoid particle for non-spherical discrete element method. Eng. Comput.
Nardelli, V., Coop, M.R., Andrade, J.E., Paccagnella, F., 2017. An experimental investigation of the micromechanics of Eglin sand. Powder Technol. 312, 166–174.
Navarro, H.A., de Souza Braun, M.P., 2013. Determination of the normal spring stiffness coefficient in the linear spring–dashpot contact model of discrete element method. Powder Technol. 246, 707–722.
Nie, Z., Fang, C., Gong, J., Liang, Z., 2020. DEM study on the effect of roundness on the shear behaviour of granular materials. Comput. Geotech. 121, 103457.
Pereira, C.M., Ramalho, A.L., Ambrósio, J.A., 2011. A critical overview of internal and external cylinder contact force models. Nonlinear Dyn. 63 (4), 681–697.
Podlozhnyuk, A., Pirker, S., Kloss, C., 2017. Efficient implementation of superquadric particles in Discrete Element Method within an open-source framework. Comput. Particle Mech. 4 (1), 101–118.
Poli, R., Kennedy, J., Blackwell, T., 2007. Particle swarm optimization. Swarm Intell. 1 (1), 33–57.
Pouchol, M., Ahmad, A., Crespin, B., Terraz, O., 2009. A hierarchical hashing scheme for nearest neighbor search and broad-phase collision detection. J. Graphics, GPU, Game Tools 14 (2), 45–59.
Rakotonirina, A.D., Delenne, J.-Y., Radjai, F., Wachs, A., 2019. Grains3D, a flexible DEM approach for particles of arbitrary convex shape – Part III: extension to non-convex particles modelled as glued convex particles. Comput. Particle Mech. 6 (1), 55–84.
Senetakis, K., Coop, M.R., Todisco, M.C., 2013. The inter-particle coefficient of friction at the contacts of Leighton Buzzard sand quartz minerals. Soils Found. 53 (5), 746–755.
Sufian, A., Russell, A.R., Whittle, A.J., 2017. Anisotropy of contact networks in granular media and its influence on mobilised internal friction. Géotechnique 67 (12), 1067–1080.
Thakur, M.M., Penumadu, D., 2020. Triaxial compression in sands using FDEM and micro-X-ray computed tomography. Comput. Geotech. 124, 103638.
Van den Bergh, F., Engelbrecht, A., 2010. A convergence proof for the particle swarm optimiser. Fundamenta Informaticae 105 (4), 341–374.
Vardoulakis, I., 1980. Shear band inclination and shear modulus of sand in biaxial tests. Int. J. Numer. Anal. Meth. Geomech. 4 (2), 103–119.
Vlahinić, I., Andò, E., Viggiani, G., Andrade, J., 2014. Towards a more accurate characterization of granular media: extracting quantitative descriptors from tomographic images. Granular Matter 16 (1), 9–21.
Voivret, C., Radjai, F., Delenne, J.-Y., El Youssoufi, M.S., 2009. Multiscale force networks in highly polydisperse granular media. Phys. Rev. Lett. 102 (17), 178001.
Wachs, A., Girolami, L., Vinay, G., Ferrer, G., 2012. Grains3D, a flexible DEM approach for particles of arbitrary convex shape – Part I: Numerical model and validations. Powder Technol. 224, 374–389.
Wang, X., Gong, J., An, A., Zhang, K., Nie, Z., 2019. Random generation of convex granule packing based on weighted Voronoi tessellation and cubic-polynomial-curve fitting. Comput. Geotech. 113, 103088.
Xia, Y., Stickel, J.J., Jin, W., Klinger, J., 2020. A review of computational models for the flow of milled biomass I: Discrete-particle models. ACS Sustainable Chem. Eng.
Zhao, S., Zhao, J., 2019. A poly-superellipsoid-based approach on particle morphology for DEM modeling of granular media. Int. J. Numer. Anal. Meth. Geomech. 43 (13), 2147–2169.
Zhao, S., Zhou, X., 2017. Effects of particle asphericity on the macro-and micro-mechanical behaviors of granular assemblies. Granular Matter 19 (2), 38.
Zhao, S., Zhou, X., Liu, W., Lai, C., 2015. Random packing of tetrahedral particles using the polyhedral discrete element method. Particuology 23, 109–117.
Zhao, S., Evans, T.M., Zhou, X., 2018. Effects of curvature-related DEM contact model on the macro-and micro-mechanical behaviours of granular soils. Géotechnique 68 (12), 1085–1098.
Zheng, J., Hryciw, R., 2017. An image based clump library for DEM simulations. Granular Matter 2 (19), 26.
Zheng, J., Hryciw, R., 2017. Soil particle size and shape distributions by stereophotography and image analysis. Geotech. Test. J. 40 (2), 317–328.
Zheng, J., Hryciw, R., Ventola, A., 2017. Compressibility of sands of various geologic origins at pre-crushing stress levels. Geotech. Geol. Eng. 35 (5), 2037–2051.
Zhong, W., Yu, A., Liu, X., Tong, Z., Zhang, H., 2016. DEM/CFD-DEM modelling of non-spherical particulate systems: theoretical developments and applications. Powder Technol. 302, 108–152.
Zhou, B., Wang, J., Wang, H., 2018. Three-dimensional sphericity, roundness and fractal dimension of sand particles. Géotechnique 68 (1), 18–30.
Zhu, H.P., Zhou, Z.Y., Yang, R.Y., Yu, A.B., 2008. Discrete particle simulation of particulate systems: a review of major applications and findings. Chem. Eng. Sci. 63 (23), 5728–5770.